

E9688
8/14/95

Thermographic Imaging for High-Temperature Composite Materials – A Defect Detection Study

Don J. Roth
Lewis Research Center
Cleveland, Ohio

James R. Bodis
Cleveland State University
Cleveland, Ohio

and

Chip Bishop
Bales Scientific, Inc.
Walnut Creek, California

June 1995



National Aeronautics and
Space Administration

Thermographic Imaging for High-Temperature Composite Materials -A Defect Detection Study

Don J. Roth

National Aeronautics and Space Administration
Lewis Research Center
Cleveland, Ohio 44135

James R. Bodis

Cleveland State University
Cleveland, Ohio 44115

Chip Bishop

Bales Scientific, Inc.
Walnut Creek, California 94595

ABSTRACT

The ability of a thermographic imaging technique for detecting flat-bottom hole defects of various diameters and depths was evaluated in four composite systems (two types of ceramic matrix composites, one metal matrix composite, and one polymer matrix composite) of interest as high-temperature structural materials. The holes ranged from 1 to 13 mm in diameter and 0.1 to 2.5 mm in depth in samples approximately 2 - 3 mm thick. The thermographic imaging system utilized a scanning mirror optical system and infrared (IR) focusing lens in conjunction with a Mercury-Cadmium-Telluride infrared detector element to obtain high resolution infrared images. High intensity flash lamps located on the same side as the infrared camera were used to heat the samples. After heating, up to 30 images were sequentially acquired at 70 - 150 msec intervals. Limits of detectability based on depth and diameter of the flat-bottom holes were defined for each composite material. Ultrasonic and radiographic images of the samples were obtained and compared with the thermographic images. This study was done under a non-reimbursable Space Act Agreement between NASA - Lewis Research Center and Bales Scientific, Inc. to allow several heating configurations to be evaluated in a cost-effective and timely fashion. The authors wish to thank Ron Cairo of Pratt & Whitney for delamination sensitivity analysis.

1. INTRODUCTION

Significant effort and resources are being expended to develop ceramic matrix (CMC), metal matrix (MMC), and polymer matrix (PMC) composites for high-temperature engine components and other parts in advanced aircraft.^{1,2} Additionally, composite structural material development is being actively pursued in other industries such as automotive and sports equipment.¹ A portion of the development effort is dedicated to the assessment of nondestructive evaluation

(NDE) technologies for detecting flaws in these materials.² To illustrate the importance of defect detection and characterization, figure 1 shows the results of a delamination sensitivity analysis on a CMC material in consideration for use as a hot section material in advanced aircraft engines. The study indicates that as the size of delaminations increases from 3 x 3 mm to 25 x 25 mm, the hot surface temperature increases by up to 50% making the material unusable for hot section application. Similarly, the study indicates that as delamination depth relative to the hot surface decreases from 1.9 to 0.6 mm, hot surface temperature increases by around 5%. It can be seen from this study that the use of these materials in engines will require nondestructive evaluation methods that can detect and accurately characterize the size and depth of defects present. Recent technological advancements in infrared camera technology and computer power have made thermographic imaging systems worth evaluating as a nondestructive evaluation tool for advanced composites. Thermography offers the advantages of real-time inspection, no contact with sample, non-ionizing radiation, complex-shape inspection capability, variable field of view size, and portability.

The objective of this study was to evaluate the ability of a thermographic imaging technique for detecting flat-bottom hole defects of various diameters and depths in 4 composite systems of interest as high-temperature structural materials. The technique utilized high intensity flash lamps to heat the sample located on the same side of the detecting infrared camera. The composite systems were (fiber/matrix): silicon carbide / calcia-alumina-silica (SiC/CAS) CMC, silicon carbide / silicon carbide (SiC/SiC) CMC, silicon carbide / titanium alloy (SiC/Ti) MMC, and graphite / polyimide PMC. The holes ranged from 1 to 13 mm in diameter and 0.1 to 2.5 mm in depth in samples approximately 2 - 3 mm thick. Ultrasonic and radiographic images of the samples were obtained and compared with the thermographic images. Additional experiments were performed to determine the effect of field of view size on detectivity of defects. This issue is critical as the aerospace industry searches for high-speed methods to inspect components in the field. As large a field of view as possible is desired because it means fewer number of inspections per component and thus reduced inspection time.

2. EXPERIMENTAL

2.1 Materials Table 1 describes the composite systems studied.

Table 1. Composite Systems Description

Composite	Thickness Range (mm)	Number of Plies	Ply Orientation	Volume Fraction Fibers	Volume Fraction Porosity
SiC/CAS CMC	2.2 - 2.5	12	unidirectional	0.35 - 0.45	0.01 - 0.02
SiC/SiC CMC	2.3 - 2.7	8	[0/90], [\pm 45], and [0/45/90/-45] _s	0.4	0.14 - 0.16
SiC/Ti MMC	1.7 - 2.1	8	unidirectional	0.35 - 0.45	0
Graphite / Polyimide PMC	2.3 - 3.0	9	unidirectional	0.50 - 0.60	0.01 - 0.02

2.2 Sample Defect Preparation The SiC/CAS CMC, SiC/Ti MMC, and Graphite / Polyimide PMC were machined to make flat bottom holes by utilizing center cutting solid carbide end mills of different diameters. The sample was fed into the cutter until reaching the desired depth. The mills were rotated between 60 - 120 RPM (the larger the mill, the lower the RPM). No coolant was used. The SiC/SiC samples required ultrasonic milling at 42 KHz with coolant to machine the flat bottom holes. The flat bottom hole defects ranged in diameter and depth for each material as shown in table 2. Defect distribution plots showing diameter versus depth will be shown in the RESULTS section when detectability results are presented. Figure 2 shows a photograph of a SiC/CAS sample with flat bottom holes. Because of the limited number of samples, and the desired sizes and depths of defects for this investigation, flat bottom holes were in some cases machined slightly closer to each other and to sample edges than preferred to avoid potential thermal interference effects. Average spacing between defects was 2 - 5 mm.

Table 2. Depth and Diameter Ranges of Flat Bottom Holes for Each Material

Material	Depth Range (mm)	Diameter Range (mm)
SiC/CAS CMC	0.1 - 2.0	1.2 - 11.4
SiC/SiC CMC	0.6 - 2.2	2.5 - 8.4
SiC/Ti MMC	0.5 - 1.9	1.5 - 13
Graphite/Polyimide PMC	0.4 - 2.5	1.4 - 11

2.3 Thermography Technique Description High energy (6400 J) xenon flash lamps located on the same side as the detecting infrared (IR) camera are flashed which triggers the IR camera to begin collecting temperature information from the surface of the sample under evaluation. Defect boundaries inside the material act to slow down (lower diffusivity material such as air gap) or speed up (material inclusion of higher conductivity than that of matrix) the diffusion of the thermal front as it propagates into the material. Due to the changed diffusion rate, temperatures will be different (higher in the case of an air gap) in the areas near the defects than in the surrounding "good" material. IR energy from the sample surface enters the camera through the front panel viewport where it impinges upon a 12-faceted mirror rotating 360° horizontally (horizontal polygon mirror) followed by a mirror angling vertically (vertical tilt mirror). After reflection off of the vertical mirror, the IR energy travels through an IR focusing lens onto a liquid nitrogen-cooled Mercury-Cadmium-Telluride IR detector element. The horizontal-vertical mirror system is synchronized such that each horizontal mirror facet is responsible for producing one full line of video data composed of 200 to 800 elements of temperature information. In this manner, a vertical frame (IR image) composed of 200 to 800 horizontal lines of temperature data is constructed. The lamp flashing and image acquisition are controlled and synchronized via a central processing unit. Two blackbody references are located

within the the scanning optical path to assure true temperature tracking. Each blackbody contains a highly accurate temperature sensor for internal calibration. Temperature resolution of the system is 0.05°C.

To a first approximation, it has been found that 1) the time at which a defect appears is proportional to the square of depth³ and 2) loss of thermal contrast (i.e., the detected temperature difference between a defective area and a sound area) is proportional to the cube of depth.⁴ An empirical rule for thermography states that defects of diameter $\leq 0.5*d - 1.0*d$ where d is the depth below the surface probably will not be detected.⁵

2.4 Experiments The SiC/Ti MMC samples were spray painted flat black to increase the emissivity of the shiny, silver metallic surface characteristic of these composites. No other samples required this paint due to their dark-colored, non-specular surface. All samples were mounted with the surface containing flat bottom holes facing away from the camera against a flat steel plate (painted black). Four heating configurations were attempted to determine their effect on detectivity (table 3). Configuration 2 is shown schematically in figure 3. The distance between sample and camera was measured and input to the computer to allow motor-driven positioning of the IR lens for optimum focusing of thermal energy on the detector element. The flash lamps were located inside parabolic aluminum reflectors to increase the amount of heat energy in the direction of the sample. For comparison of the power of the different heating methods, the last column of table 3 shows the resulting maximum surface temperatures achieved (as determined from the first frame of acquired image data) by each configuration for a SiC/CAS sample.

Table 3. Heating Configurations Used in This Study

Heating Configuration	Number of Flash Lamps	Flash Lamp-to-Sample Distance (cm)	Camera-to-Sample Distance (cm)	Angle Between Sample and Flash Lamps (degrees)	Resulting Maximum Surface Temperature of SiC/CAS sample Acquired in First Frame After Heating (°C)
1	2 (unpolished parabolic reflectors encompassing xenon bulbs)	25	25	30	111
2	2 (polished parabolic reflectors encompassing xenon bulbs)	20	20	45	206
3	4 (unpolished parabolic reflectors encompassing xenon bulbs)	38	38	45	88
4	4 (polished parabolic reflectors encompassing xenon bulbs) arranged in linear array	38	38	20	138

Up to 30 IR image frames were acquired sequentially at 100 - 200 msec intervals after flashing. In cases where defects were not detected through 30 frames using the 100 - 200 msec delay time, 500 msec delay intervals were tried.

Detectability studies were accomplished by an individual with 20/20 vision viewing thermography image frames on a 1024 x 768 pixel resolution monitor of 40.5 cm diagonal. The actual image sizes on video were automatically calculated by the computer and generally 6 - 12 cm horizontal dimension by 6 - 8 cm vertical dimension. The camera was set to zoom in on the field of view so that the sample area for detectability determinations was optimized (except for the later experiments in which detectability was determined as a function of field of view size). A contrast expansion method was applied to the obtained thermography image frames to optimize the detectability of the defects. The method involved mapping a gray scale shade (110 possible shades) to every temperature increment of 0.05 °C between the minimum and maximum temperatures in the image. When more than 110 discrete temperatures (in increments of 0.05 °C) are present in the image, the gray shading "wraps around" or begins again from the first shade used. Detection was defined as being able to resolve individual defects. Defects were classified as "not detected," "barely detected," or "detected" with "barely detected" indications showing the threshold of detectability. Barely-detected defects were counted as "detected" in tables 5 - 8 presented in the RESULTS section. A reliability of detection study⁶ requiring statistically significant defect populations was not performed here due to the large expense of manufacturing and machining the advanced composite materials.

Additional experiments were performed to determine the effect of field of view size (as determined by the distance of the IR camera from the sample) on detectability of defects. For the latter experiments, sample-to-camera distance was increased from 40 to 160 cm in increments of 20 cm so that the field of view (lateral dimension) increased from 14 to 44 cm in increments of 5 cm.

2.5 Further NDE Characterization Ultrasonic and radiographic imaging were performed on the samples to compare with the thermographic imaging results. Table 4 describes the further NDE characterization performed.

Table 4. Description of Further NDE Characterization

Material	Ultrasonic C-scan Imaging	Conventional Film Radiographic Imaging (Sample in Direct Contact With Film)
SiC/CAS CMC	<ul style="list-style-type: none"> * Type = Pulse-echo * Transducer = Focused 10 Mhz Longitudinal Wave * Gates on Front-surface echo (trailing edge), back-surface echo, and intermediate time location between front and back surface echoes * 512 x 319 scan points w/ 0.206 mm increment between points 	<ul style="list-style-type: none"> * Voltage = 70 KV * Source-to-Sample Distance = 120 cm * Current = 9.15 mA * Exposure Time = 20 sec
SiC/SiC CMC	<ul style="list-style-type: none"> * Type = Pulse-echo * Transducer = Focused 5 Mhz Longitudinal Wave * Gates on Front-surface echo (trailing edge), back-surface echo, and intermediate time location between front and back surface echoes * 512 x 67 scan points w/ 0.333 mm increment between points <hr/> <ul style="list-style-type: none"> * Type = Through- transmission * Transducers = Focused 10 Mhz Longitudinal Wave Sender and Unfocused 10 Mhz Longitudinal Wave Receiver * Gates on several through-transmitted echoes * 918 x 180 scan points w/ 0.175 mm increment between points 	<ul style="list-style-type: none"> * Voltage = 70 KV * Source-to-Sample Distance = 120 cm * Current = 9.15 mA * Exposure Time = 30 sec
SiC/Ti MMC	<ul style="list-style-type: none"> * Type = Pulse-echo * Transducer = Focused 10 Mhz Longitudinal Wave * Gates on Front-surface echo (trailing edge), back-surface echo, and intermediate time location between front and back surface echoes * 512 x 412 scan points w/ 0.159 mm increment between points 	<ul style="list-style-type: none"> * Voltage = 70 KV * Source-to-Sample Distance = 120 cm * Current = 9.15 mA * Exposure Time = 120 sec
Graphite/Polyimide PMC	<ul style="list-style-type: none"> * Type = Pulse-echo * Transducer = Focused 10 Mhz Longitudinal Wave * Gates on Front-surface echo (trailing edge), back-surface echo, and intermediate time location between front and back surface echoes * 512 x 224 scan points w/ 0.175 mm increment between points 	<ul style="list-style-type: none"> * Voltage = 70 KV * Source-to-Sample Distance = 120 cm * Current = 9.15 mA * Exposure Time = 20 sec

3. RESULTS AND DISCUSSION

All quantitative detectability results shown are those obtained with heating configuration 2 (table 3). The depths and diameters given in figures 4, 6, 8, and 10 have ± 50 μm and ± 10 μm measurement error, respectively.

3.1 SiC/CAS CMC Figure 4 and table 5 show the detectability results for the SiC/CAS samples. Based on these data, defects of depth ≥ 1.8 mm with diameters ≤ 1.6 mm in this SiC/CAS material probably will not be detected with the thermography methodology used in this study. This result is consistent with the empirical rule that states that defects of diameter $\leq 0.5*d - 1.0*d$ where d is the depth below the surface probably will not be detected.

Table 5. Thermography Detectability Data for SiC/CAS
Ceramic Matrix Composite

Defect Diameter Range (mm)	Depths over which defects of specified diameter range were detected (mm)	Depths over which defects of specified diameter range were <i>not</i> detected (mm)
0 - 2	≤ 1.6	≥ 1.8
2 - 4	≤ 1.8	none
4 - 6	≤ 1.9	none
6 - 8	≤ 1.9	none
8 - 10	≤ 1.9	none
10 - 12	≤ 2	none

Figure 5 shows a time sequence of thermography images for a SiC/CAS sample containing defects. The images are separated by 250 ± 30 msec (time of 3 frame acquisitions plus delay time between frames) and illustrate the detection of defects as function of time after heating. The shallower defects ($0.9 \text{ mm} \leq \text{depth} \leq 1.1 \text{ mm}$) began to appear approximately 250 - 450 msec after heating with high contrast obtained at times ≥ 500 msec. The deeper defects ($1.5 \text{ mm} \leq \text{depth} \leq 1.6 \text{ mm}$) began to appear approximately 850 msec after heating with high contrast obtained at times 1200 msec - 1500 msec. The deeper defects tend to appear more diffuse than the shallower defects when comparing the frames for each where maximum contrast occurred.

Figure 6 shows radiographic and pulse-echo ultrasonic c-scan (gated front surface echo trailing edge) images of the same SiC/CAS sample. The defects were clearly detected in the radiograph. All defects were detected in the ultrasonic image although the smaller, shallower indications overlap with each other due to ultrasonic interference.

3.2 SiC/SiC CMC Figure 7 and table 6 show the detectability results for the SiC/SiC samples. Based on these data, defects of depth ≥ 1.8 mm with diameters ≤ 2.6 mm in this

SiC/SiC material probably will not be detected with the thermography methods of this study. This result is consistent with the empirical rule that states that defects of diameter $\leq 0.5*d$ - $1.0*d$ where d is the depth below the surface probably will not be detected.

Table 6. Thermography Detectability Data for SiC/SiC Ceramic Matrix Composite

Defect Diameter Range (mm)	Depths over which defects of specified diameter range were detected (mm)	Depths over which defects of specified diameter range were <i>not</i> detected (mm)
0 - 1	N/A	N/A
1 - 2	N/A	N/A
2 - 3	≤ 1.5	≥ 1.8
3 - 4	≤ 1.9	none
4 - 5	≤ 1.9	none
5 - 6	≤ 1.9	none
6 - 8	N/A	N/A
8 - 9	≤ 1.9	none

Figure 8 shows thermography images for a SiC/SiC sample containing defects. The images correspond to the times after heating where maximum contrast occurred for defects of depths 0.8 - 1 mm (figure 8a, time = 310 ± 20 msec) and depths of 1.2 - 1.5 mm (figure 8b, time = 620 ± 40 msec). As with the SiC/CAS material, the deeper defects appear later in time after heating and are more diffuse in appearance than the shallower defects. Detectability did not appear to be affected by ply layup as detectability results were similar for 0/90, ± 45 , and 0/+45/90/-45 layups.

Figure 9 shows pulse-echo ultrasonic c-scan (gated back surface echo), through-transmission ultrasonic c-scan and radiographic images of the same SiC/SiC sample. Radiographic images clearly show all defects. The pulse-echo c-scan image (back-wall reflection) show indications of the shallowest and intermediate depth defects but in a diffuse, ambiguous manner. Through-transmission c-scan images show all the defects but they cannot be individually resolved due to ultrasonic interference.

3.3 SiC / Ti MMC Figure 10 and table 7 show the detectability results for the SiC/Ti samples. Based on these data, defects of depth ≥ 1.6 mm with diameters ≤ 3.2 mm in this SiC/Ti material probably will not be detected with the thermography methodology of this study. This result is consistent with the empirical rule that states that defects of diameter $\leq 0.5*d$ - $1.0*d$ where d is the depth below the surface probably will not be detected.

Table 7. Thermography Detectability Data for SiC/Ti
Metal Matrix Composite

Defect Diameter Range (mm)	Depths over which defects of specified diameter range were detected (mm)	Depths over which defects of specified diameter range were <i>not</i> detected (mm)
0 - 2	≤ 1.6	≥ 1.7
2 - 4	≤ 1.5	≥ 1.6
4 - 6	N/A	N/A
6 - 8	≤ 1.6	≥ 1.6
8 - 10	≤ 1.8	N/A
10 - 12	≤ 1.8	N/A

Figure 11 shows a time sequence of thermography images for a SiC/Ti sample containing defects. The images are separated by 180 ± 20 msec and illustrate the detection of defects as function of time after heating. The shallower defects ($0.5 \text{ mm} \leq \text{depth} \leq 0.7 \text{ mm}$) began to appear with high contrast at times approximately 200 msec after heating. Some of the larger ($\sim 6 - 13 \text{ mm}$ in diameter) defects at the deeper depths ($1.6 \text{ mm} \leq \text{depth} \leq 1.7 \text{ mm}$) appear with maximum contrast approximately 600 msec after heating. The smallest ($\sim 1 - 3 \text{ mm}$ in diameter) defects at these depths were not detected.

Figure 12 shows the radiographic and pulse-echo ultrasonic c-scan (gated back surface echo) images of the same SiC/Ti sample. All defects are detected in both images, although the deepest, smallest ones appear with slightly less clarity in the ultrasonic image.

3.4 Graphite / Polyimide PMC Figure 13 and table 8 show the detectability results for the Graphite/Polyimide samples. The detectability results indicate that defects of all diameters ($1 \text{ mm} - 12 \text{ mm}$) $\geq 1.8 \text{ mm}$ in depth were not detected, i.e. depth appears to be the limiting variable with regards to detectability. Based on these data, defects of depth $\geq 1.6 \text{ mm}$ in this Graphite/Polyimide material probably will not be detected with the thermography methods used in this study. This definitive depth boundary demarcating detectability (for the diameters studied here) contrasts with those for the CMC and MMC systems where a detectability threshold based solely on depth was not obviously apparent. Hence, detectability is qualitatively "more difficult" in PMC materials than for the CMC and MMC materials. This conclusion, consistent with previous studies on carbon-fiber reinforced plastics,⁷ is likely due to the fact that the thermal conductivity in the plane of the material is an order of magnitude greater than that through the thickness leading to low propagation of the thermal front in the thickness direction and rapid loss of contrast.⁸ Had thicker samples containing deeper defects been available for the CMC and MMC materials, it is speculated that a depth threshold of detectability may have been observed that was greater than that seen for the PMC. The data shown in figure 13 are consistent with the empirical rule that states that defects of diameter $\leq 0.5*d - 1.0*d$ where d is the depth below the surface probably will not be detected.

Table 8. Thermography Detectability Data for Graphite/Polyimide Polymer Matrix Composite

Defect Diameter Range (mm)	Depths over which defects of specified diameter range were detected (mm)	Depths over which defects of specified diameter range were <i>not</i> detected (mm)
0 - 2	≤ 1.4	≥ 1.8
2 - 4	≤ 1.2	≥ 1.8
4 - 6	≤ 1.1	≥ 1.8
6 - 8	N/A	N/A
8 - 10	≤ 1.1	≥ 1.8
10 - 12	≤ 1.1	≥ 1.8

Figure 14 shows a time sequence of thermography images for a graphite/polyimide sample containing defects. The images are separated by 85 ± 10 msec (time of single frame acquisition plus delay time between frames) and illustrate the detection of defects as function of time after heating. Only the shallowest defects ($0.7 \text{ mm} \leq \text{depth} \leq 0.8 \text{ mm}$) in the sample appear in the images. These defects begin to appear faintly at times 150 - 350 msec and with high contrast at times ≥ 400 msec. The deeper defects ($1.8 \text{ mm} \leq \text{depth} \leq 2.0 \text{ mm}$), as large as $\sim 12 \text{ mm}$ in diameter, were never visible at any time.

Figure 15 shows the pulse-echo ultrasonic c-scan (gated back surface echo) and radiographic images of the same graphite/polyimide sample. All defects are clearly detected in the radiograph. In the ultrasonic image, the shallow row of defects is detected while the deeper row of defects shows semicircular indications towards the bottom of the row but is mostly hidden due to ultrasonic scatter.

3.5 Effect of Heating Configuration (Initial Surface Temperature) on Detectability The initial surface temperature affected the results with regards to the detectability of the deepest and smallest defects in the samples. For example, as shown in figure 16, a 3.0 mm diameter defect located $\sim 1.7 \text{ mm}$ below the surface in a SiC/CAS sample could be detected using heating configuration 2 (maximum surface temperature in first frame after heating = 206°C) but not using heating configuration 1 (maximum surface temperature in first frame after heating = 111°C). Additionally, most of the deeper defects were seen more clearly (with more contrast) using the configurations resulting in higher initial surface temperatures (more powerful heating).

3.6 Effect of Field of View Size on Defect Detectivity Figure 17 show a sequence of images where the camera-to-sample distance was varied from 40 cm to 160 cm for one of the SiC/CAS samples, which correspondingly increased the field of view (FOV) size (lateral dimension) from 14 to 44 cm. As the field of view is increased in size, the sample becomes a

smaller portion of it. Only the sample (rather than the entire FOV including sample) is shown in figures 17a - h. Figure 18 shows the detectability results for the defects in this sample as a function of FOV lateral dimension. The shallower defects ($0.6 \text{ mm} \leq \text{depth} \leq 0.8 \text{ mm}$) ranging in diameter from 3.0 - 11.5 mm in diameter were detected at all FOVs. The smallest diameter (1.5 mm) defect in this depth range could not be detected at FOVs $\geq 29 \text{ cm}$ (sample-to-camera distance $\geq 100 \text{ cm}$). For the greater depth range ($1.6 \text{ mm} \leq \text{depth} \leq 1.8 \text{ mm}$), the 9.0 and 10.5 mm defects were detected at all FOVs while those defects ranging in diameter from 1.5 to 6.0 mm became undetectable beyond certain FOVs.

4. CONCLUSIONS

The ability of a thermographic imaging technique for detecting flat-bottom hole defects of various diameters and depths was evaluated in 4 composite systems (two types of ceramic matrix composites, one metal matrix composite, and one polymer matrix composite) of interest as high-temperature structural materials. The holes ranged from 1 to 13 mm in diameter and 0.1 to 2.5 mm in depth in samples approximately 2 - 3 mm thick. The thermographic imaging system utilized a scanning mirror optical system and infrared (IR) focusing lens in conjunction with a Mercury-Cadmium-Telluride infrared detector element to obtain high resolution infrared images. High intensity flash lamps located on the same side as the infrared camera were used to heat the samples. After heating, up to 30 images were sequentially acquired at 70 - 150 msec intervals.

Limits of detectability based on depth and diameter of the flat-bottom holes were observed for each composite material. For the SiC/CAS CMC samples, defects of depth $\leq 1.8 \text{ mm}$ with diameters $\geq 1.6 \text{ mm}$ probably will be detected with the thermography methodology used in this study. For the SiC/SiC CMC samples, defects of depth $\leq 1.8 \text{ mm}$ with diameters $\geq 2.6 \text{ mm}$ probably will be detected. For the SiC/Ti MMC samples, defects of depth $\leq 1.6 \text{ mm}$ with diameters $\geq 3.2 \text{ mm}$ probably will be detected. For the graphite/polyimide PMC samples, defects of diameters $\sim 1 \text{ mm} - 12 \text{ mm}$ in depth $\leq 1.8 \text{ mm}$ probably will be detected. Depth appears to be the limiting variable with regards to detectability in the PMC system. The thermography imaging results were consistent with the empirical rule that states defects of diameter $\leq 0.5*d - 1.0*d$ where d is the depth below the surface probably will not be detected.

The thermographic images were compared with ultrasonic and conventional film radiographic images. Radiographic images clearly revealed all flat bottom holes and provided the highest quality images of the three imaging methods. The ultrasonic imaging results were material dependent. For the SiC/CAS CMC material, thermographic imaging revealed defects as clearly or more clearly than did ultrasonic imaging. For the SiC/SiC CMC material, pulse-echo ultrasonic imaging had difficulty clearly revealing all defects while through-transmission ultrasonic imaging enabled visualization of all defects; thermographic images revealed the shallowest and intermediate depth defects but could not reveal the deepest defects (those at depths $\geq \sim 2.0 \text{ mm}$ below the surface). For the SiC/Ti MMC material, ultrasonic imaging revealed all defects while thermographic images did not reveal the smallest, deepest defects (those 1 - 3 mm in diameter at depths 1.6 - 1.7 mm below the surface). For the

graphite/polyimide PMC material, ultrasonic images barely revealed indications of the deepest defects (≥ 1.8 mm below surface, $\sim 1 - 12$ mm in diameter) while thermographic images did not reveal any of the deepest defects.

5. REFERENCES

1. National Advanced Composites Strategic Plan, September 1991.
2. H. R. Gray and C. A. Ginty: Overview of NASA's Advanced High Temperature Engine Materials Technology Program. Proceedings of the 7th Annual HITEMP Review (NASA CP-10146), 1994. pp. 1-1 to 1-25.
3. P. Cielo, X. Maldague, A.A. Deom and R. Lewak: Thermographic Nondestructive Evaluation of Industrial Materials and Structures. *Mater Eval*, Vol. 43, No. 6, 1987, pp. 452 - 460.
4. J. Allport and J. McHugh: Quantitative Evaluation of Transient Video Thermography. Review of Progress in Quantitative Nondestructive Evaluation, Vol. 8A, 1988, New York, Plenum Press, pp. 253 - 262.
5. V. Vavilov and R. Taylor: Theoretical and Practical Aspects of the Thermal Nondestructive Testing of Bonded Structures. Research Techniques in NDT, Vol. V, 1982, Academic Press, pp. 238 - 279.
6. D. J. Roth and G.Y. Baaklini: Reliability of Scanning Laser Acoustic Microscopy for Detecting Internal Voids in Structural Ceramics, *Adv. Ceram. Mater.*, Vol. 1, No. 3, 1986.
7. V. Vavilov, X. Maldague, B. Dufort, F. Robitaille and J. Picard: Thermal Nondestructive Testing of Carbon Epoxy Composites: Detailed Analysis and Data Processing. *NDT&E International*, Vol. 26, No.2, 1993, p. 89.
8. W. N. Reynolds: Thermographic Methods Applied to Industrial Materials. *Canadian J. Phys.*, Vol. 64, No. 9, 1986, p. 1150.

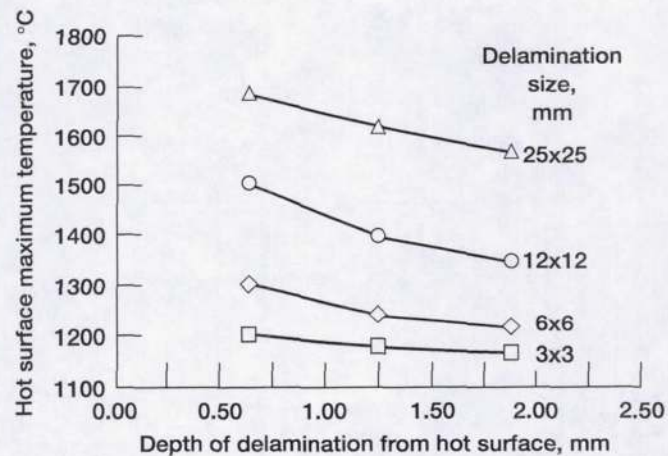


Figure 1.—Delamination thermal sensitivity study for CMC material (panel thickness = 2.5 mm, no heat transfer across delamination surfaces).

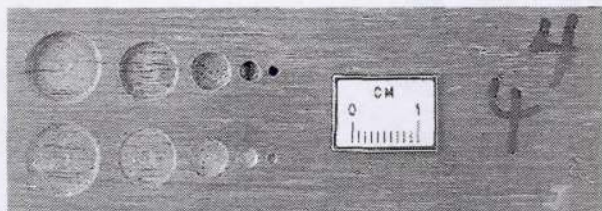


Figure 2.—Photograph of SiC/CAS CMC sample showing flat bottom holes.

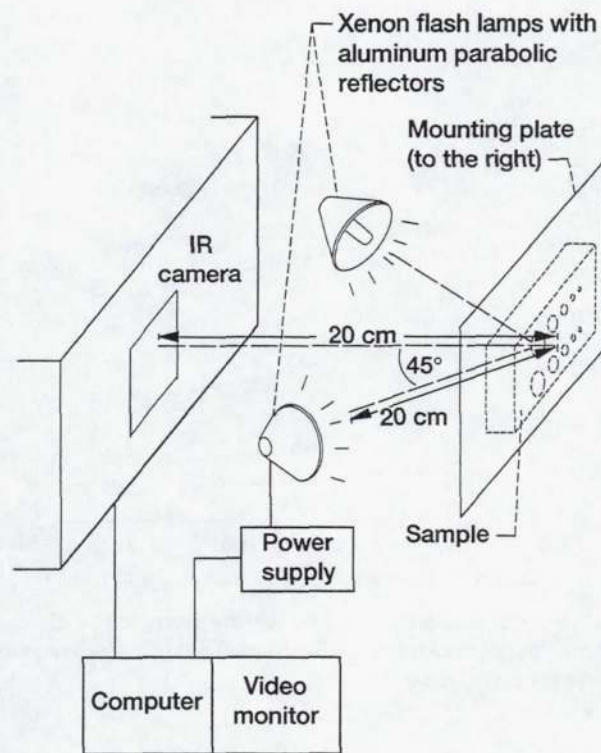


Figure 3.—Schematic of experimental configuration 2 (see table 3).

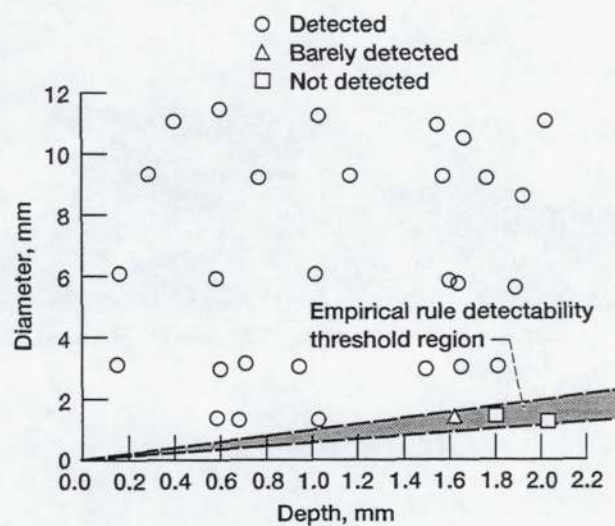


Figure 4.—SiC/CAS CMC defect distribution and thermography detectability data.

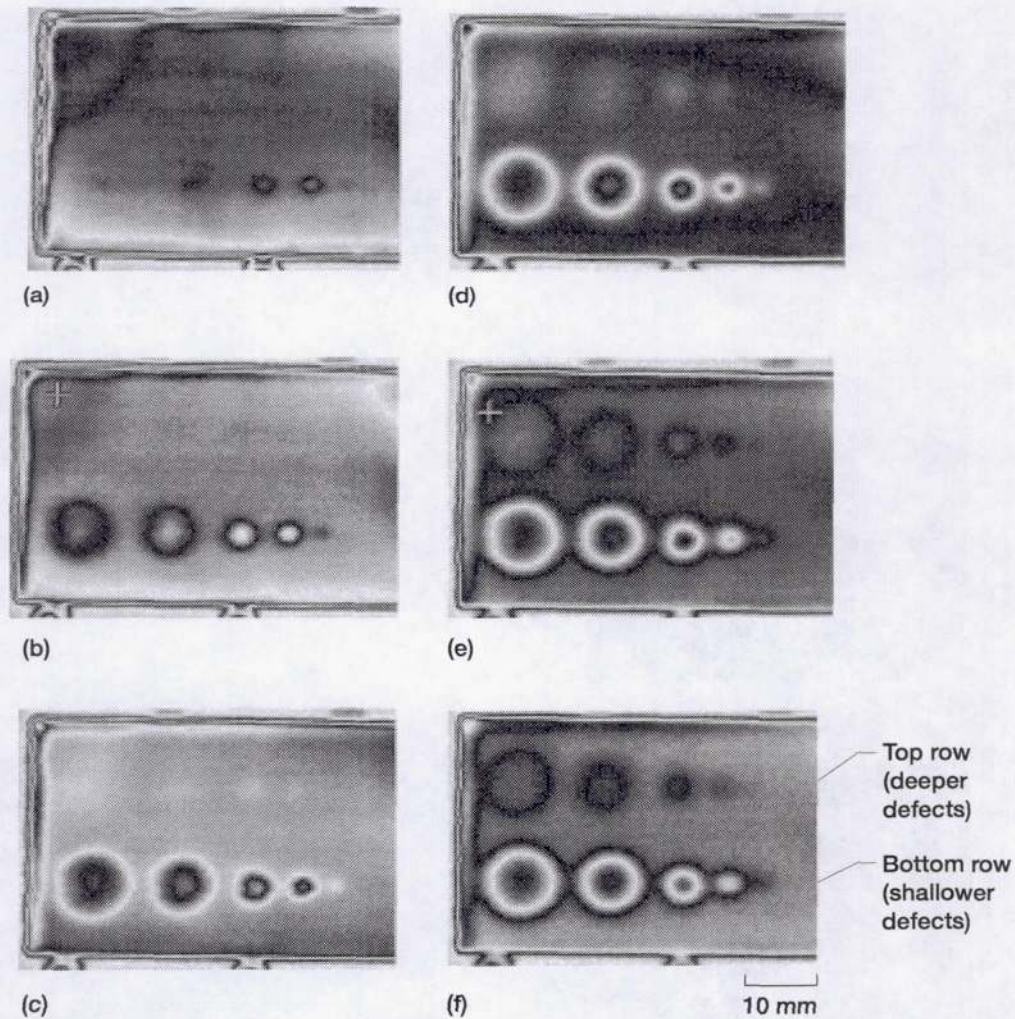


Figure 5.—Time sequence of thermography images for SiC/CAS CMC sample (time \equiv time after heating with flash lamps). Bottom row of defects at $0.9 \text{ mm} \leq \text{depth} \leq 1.1 \text{ mm}$. Top row of defects at $1.5 \text{ mm} \leq \text{depth} \leq 1.6 \text{ mm}$. (a) Time = 250 msec. (b) Time = 500 msec. (c) Time = 750 msec. (d) Time = 1000 msec. (e) Time = 1250 msec. (f) Time = 1500 msec.

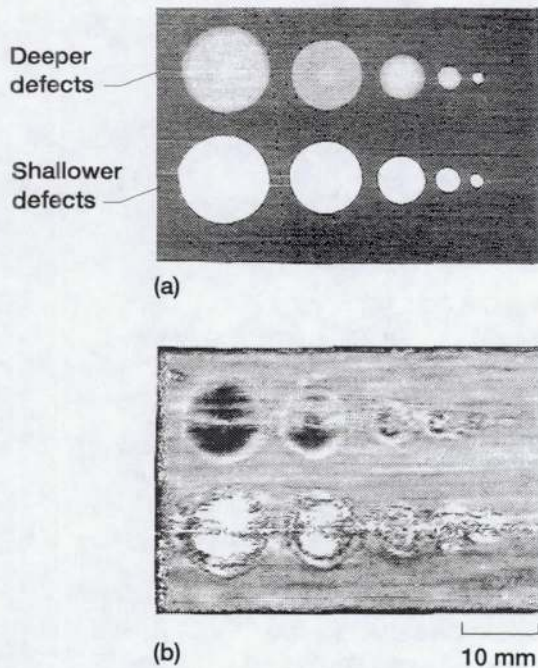


Figure 6.—Radiographic and ultrasonic images of SiC/CAS CMC sample shown in thermographic images of Figure 5. Shallower defects at $0.9 \text{ mm} \leq \text{depth} \leq 1.1 \text{ mm}$. Deeper defects at $1.5 \text{ mm} \leq \text{depth} \leq 1.6 \text{ mm}$. (a) X-ray film radiograph. (b) Pulse-echo ultrasonic image (gate on front-surface echo trailing edge).

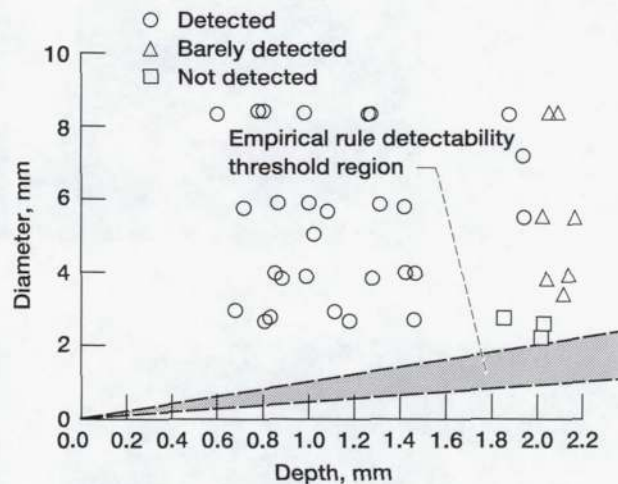


Figure 7.—SiC/SiC CMC defect distribution and thermography detectability data.

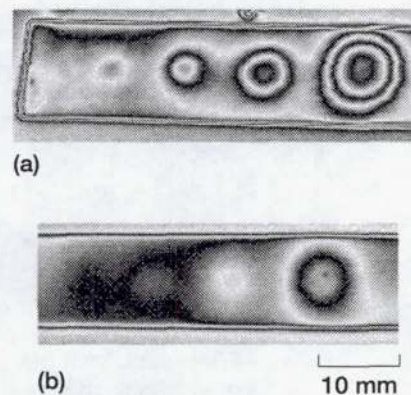


Figure 8.—Thermography images of SiC/SiC CMC sample (time \approx time after heating with flash lamps). (a) Defects at $0.8 \text{ mm} \leq \text{depth} \leq 1.0 \text{ mm}$ at time = 310 msec (maximum contrast). (b) Defects at $1.2 \text{ mm} \leq \text{depth} \leq 1.5 \text{ mm}$ at time = 620 msec (maximum contrast).

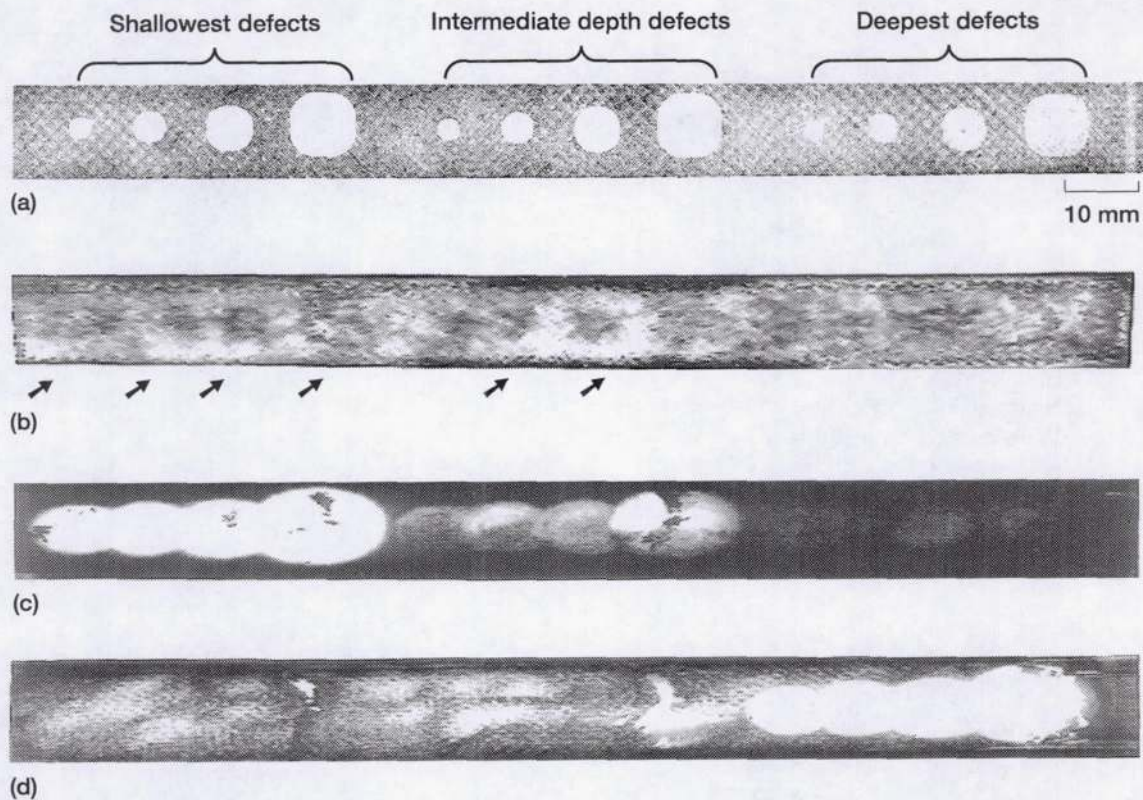


Figure 9.—Radiographic and ultrasonic images of SiC/SiC CMC sample shown in thermographic images of Figure 8. Shallowest defects at $0.8 \text{ mm} \leq \text{depth} \leq 1.0 \text{ mm}$. Intermediate depth defects at $1.2 \text{ mm} \leq \text{depth} \leq 1.5 \text{ mm}$. Deepest defects at $\text{depth} \geq 1.8 \text{ mm}$. (a) X-ray film radiograph. (b) Pulse-echo ultrasonic image (gate on back-surface echo). Only shallowest and some intermediate depth defects appear with some clarity as indicated with arrows. (c) Through-transmission ultrasonic image (gate on first major through-transmitted pulse). Shallowest and intermediate depth defects detected although overlap is seen for the indications. (d) Through-transmission ultrasonic image (gate on second major through-transmitted pulse located $\sim 2 \mu\text{sec}$ later in time than first major through-transmitted echo). Deepest depth defects detected. (Note that the defect indications in images of (c) and (d) are distorted laterally due to graphic manipulation in scaling of images (a)-(d). In the unscaled images of (c) and (d), the defects appeared circular.)

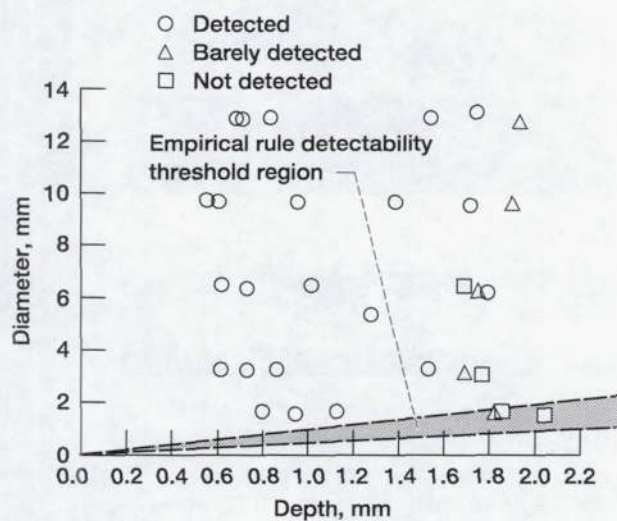


Figure 10.—SiC/Ti MMC defect distribution and thermography detectability data.

Shallower defects are clearly seen



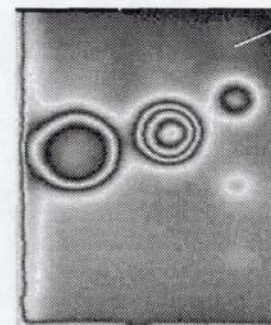
(a)

Deeper defect indications



(b)

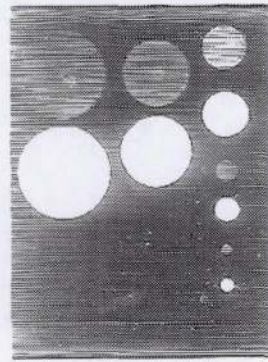
Deeper defect indications



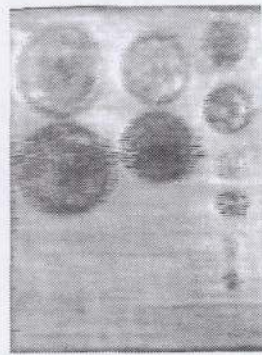
(c)

10 mm

Figure 11.—Time sequence of thermography images for SiC/Ti MMC sample (time = time after heating with flash lamps). Shallower defects ($0.5 \text{ mm} \leq \text{depth} \leq 0.7 \text{ mm}$) visible in all frames. Deeper defects ($1.6 \text{ mm} \leq \text{depth} \leq 1.7 \text{ mm}$) begin to appear with low contrast in (b). (a) Time = 270 msec. (b) Time = 450 msec. (c) Time = 630 msec.



(a) 10 mm



(b) 10 mm

Figure 12.—Radiographic and ultrasonic images of SiC/Ti MMC sample shown in Figure 11. Shallower defects at $0.5 \text{ mm} \leq \text{depth} \leq 0.7 \text{ mm}$. Deeper defects at $1.6 \text{ mm} \leq \text{depth} \leq 1.7 \text{ mm}$. Shallower defects appear white in radiograph. (a) X-ray film radiograph. (b) Pulse-echo ultrasonic image (gate on back-surface echo).

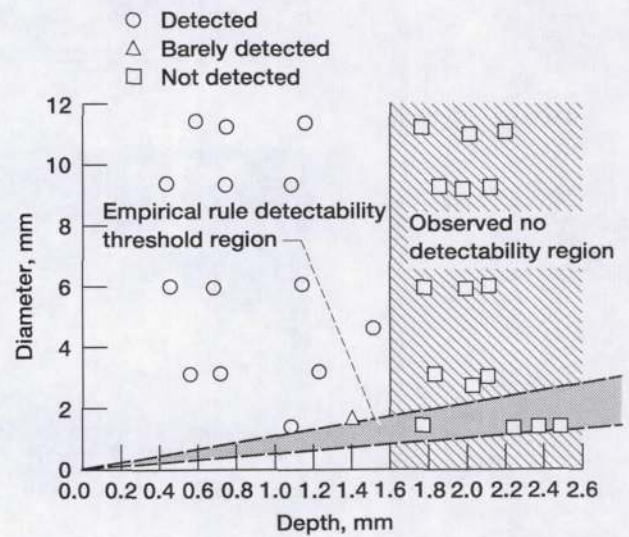
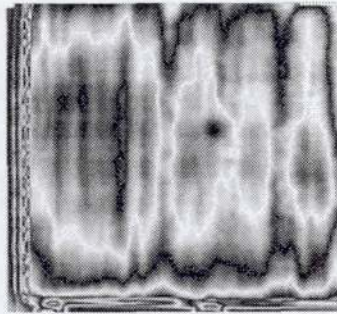
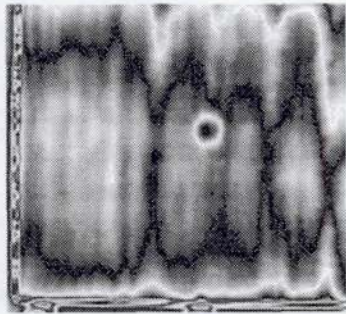


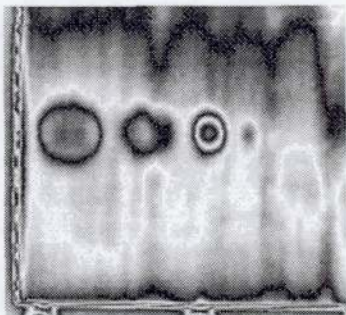
Figure 13.—Graphite/polyimide PMC defect distribution and thermography detectability data.



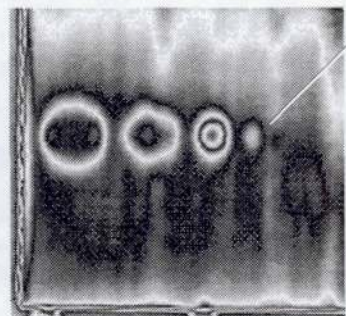
(a)



(b)



(c)



(d)

10 mm

0.3 mm diameter defect is smallest
diameter defect detected for
depth = 0.7 mm

Figure 14.—Time sequence of thermography images for graphite/polyimide PMC sample (time \approx time after heating with flash lamps). Only shallowest defects ($0.7 \text{ mm} \leq \text{depth} \leq 0.8 \text{ mm}$) detected. The deepest defects ($1.8 \text{ mm} \leq \text{depth} \leq 2.0 \text{ mm}$) were never detected at any time.
(a) Time = 150 msec. (b) Time = 300 msec. (c) Time = 450 msec.
(d) Time = 600 msec.

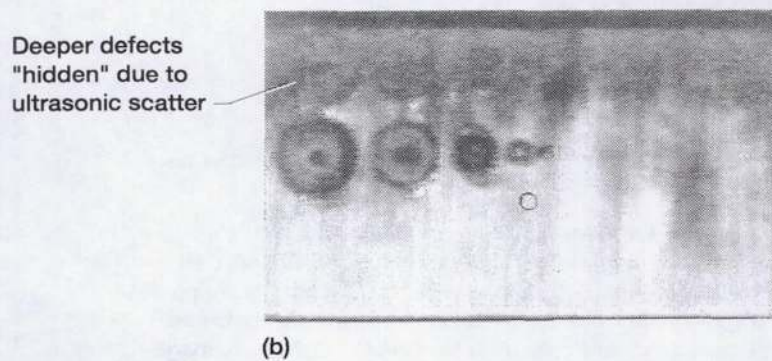
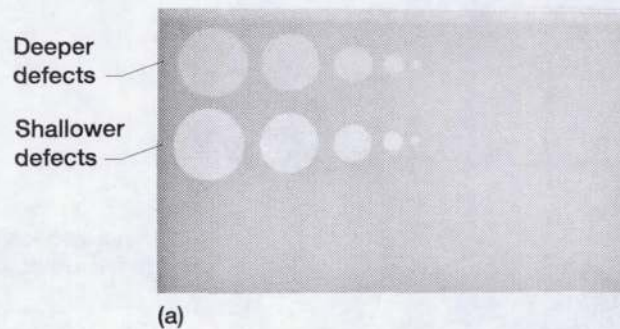
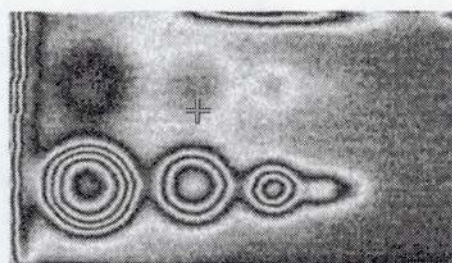
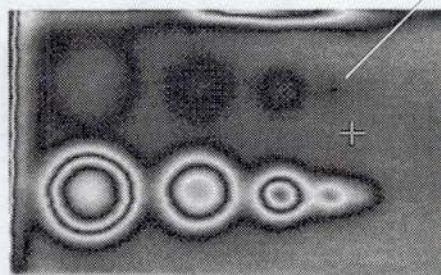


Figure 15.—Radiographic and ultrasonic images of graphite/polyimide PMC sample shown in thermographic images of Figure 14. Shallower defects at $0.7 \text{ mm} \leq \text{depth} \leq 0.8 \text{ mm}$. Deeper defects at $1.8 \text{ mm} \leq \text{depth} \leq 2.0 \text{ mm}$. (a) X-ray film radiograph. (b) Pulse-echo ultrasonic image (gate on back-surface echo).



(a)

Defect of 3.0 mm
diameter at depth of
1.7 mm is detected



(b)

Figure 16.—Effect of heating configuration (initial surface temperature) on defect detectability for SiC/CAS CMC sample. (a) Image obtained with heating configuration 1 1870 sec after heating (maximum surface temperature acquired in first frame after heating = 111 °C). (b) Image obtained with heating configuration 2 1870 sec after heating (maximum surface temperature acquired in first frame after heating = 206 °C).

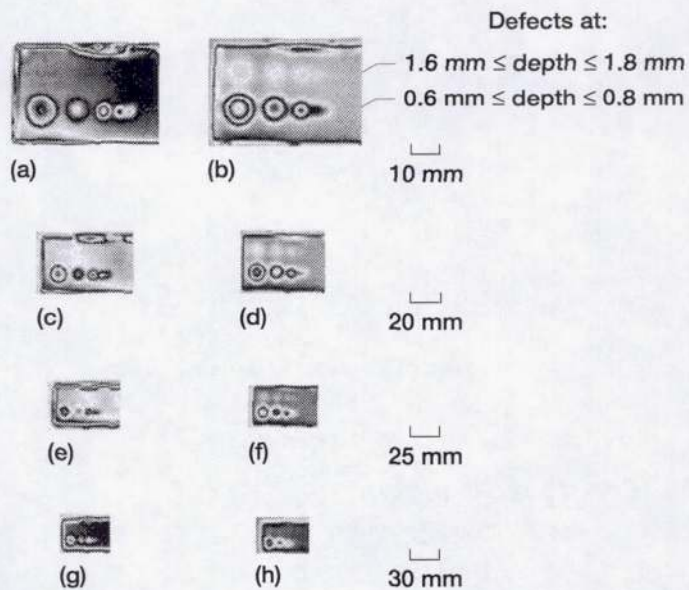


Figure 17.—Effect of field of view size on defect detectability for SiC/CAS CMC sample (time \approx time after heating with flash lamps). FOV = field of view lateral dimension. Only the sample (rather than entire field of view including sample) is shown in figures. (a) FOV = 14 cm; time = 500 msec. (b) FOV = 14 cm; time = 900 msec. (c) FOV = 24 cm; time = 500 msec. (d) FOV = 24 cm; time = 900 msec. (e) FOV = 34 cm; time = 500 msec. (f) FOV = 34 cm; time = 900 msec. (g) FOV = 44 cm; time = 500 msec. (h) FOV = 44 cm; time = 900 msec.

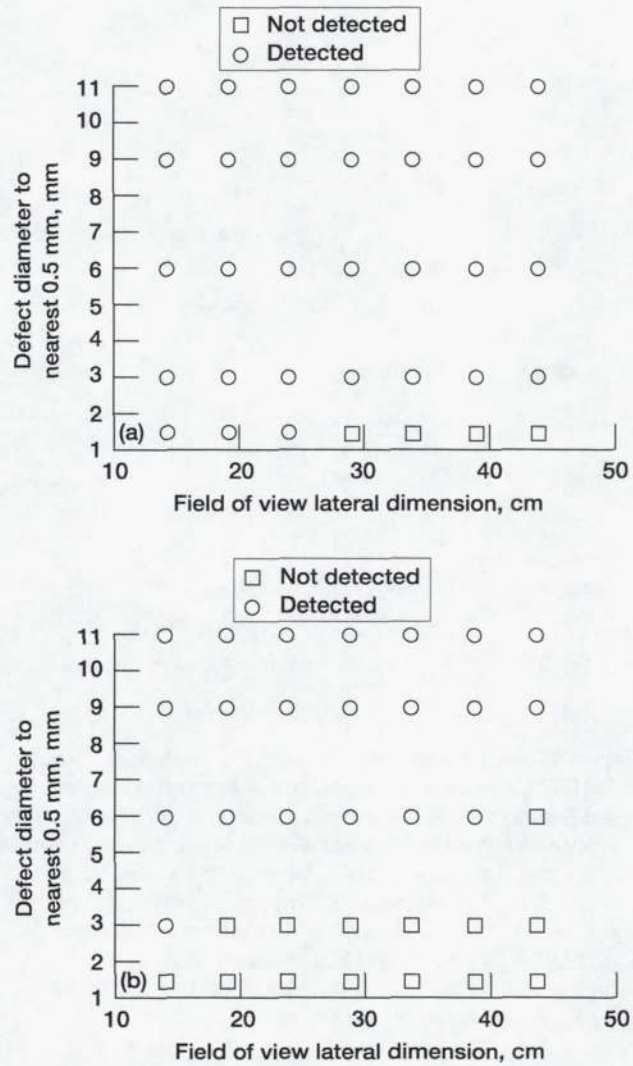


Figure 18.—Defect detectability versus field of view size for defects in SiC/CAS CMC. (a) $0.6 \leq \text{depth} \leq 0.8$ mm. (b) $1.6 \leq \text{depth} \leq 1.8$ mm.

REPORT DOCUMENTATION PAGE

Form Approved
OMB No. 0704-0188

Public reporting burden for this collection of information is estimated to average 1 hour per response, including the time for reviewing instructions, searching existing data sources, gathering and maintaining the data needed, and completing and reviewing the collection of information. Send comments regarding this burden estimate or any other aspect of this collection of information, including suggestions for reducing this burden, to Washington Headquarters Services, Directorate for Information Operations and Reports, 1215 Jefferson Davis Highway, Suite 1204, Arlington, VA 22202-4302, and to the Office of Management and Budget, Paperwork Reduction Project (0704-0188), Washington, DC 20503.

1. AGENCY USE ONLY (Leave blank)		2. REPORT DATE June 1995	3. REPORT TYPE AND DATES COVERED Technical Memorandum	
4. TITLE AND SUBTITLE Thermographic Imaging for High-Temperature Composite Materials - A Defect Detection Study			5. FUNDING NUMBERS WU-505-63-12	
6. AUTHOR(S) Don J. Roth, James R. Bodis, and Chip Bishop				
7. PERFORMING ORGANIZATION NAME(S) AND ADDRESS(ES) National Aeronautics and Space Administration Lewis Research Center Cleveland, Ohio 44135-3191			8. PERFORMING ORGANIZATION REPORT NUMBER E-9688	
9. SPONSORING/MONITORING AGENCY NAME(S) AND ADDRESS(ES) National Aeronautics and Space Administration Washington, D.C. 20546-0001			10. SPONSORING/MONITORING AGENCY REPORT NUMBER NASA TM-106950	
11. SUPPLEMENTARY NOTES Don J. Roth, NASA Lewis Research Center, James R. Bodis Cleveland State University, Cleveland, Ohio 44115, and Chip Bishop, Bales Scientific, Inc., Walnut Creek, California 94595. Responsible person, Don J. Roth, organization code 5250, (216) 433-6017.				
12a. DISTRIBUTION/AVAILABILITY STATEMENT Unclassified - Unlimited Subject Category 38 This publication is available from the NASA Center for Aerospace Information, (301) 621-0390.			12b. DISTRIBUTION CODE	
13. ABSTRACT (Maximum 200 words) The ability of a thermographic imaging technique for detecting flat-bottom hole defects of various diameters and depths was evaluated in four composite systems (two types of ceramic matrix composites, one metal matrix composite, and one polymer matrix composite) of interest as high-temperature structural materials. The holes ranged from 1 to 13 mm in diameter and 0.1 to 2.5 mm in depth in samples approximately 2 - 3 mm thick. The thermographic imaging system utilized a scanning mirror optical system and infrared (IR) focusing lens in conjunction with a Mercury-Cadmium-Telluride infrared detector element to obtain high resolution infrared images. High intensity flash lamps located on the same side as the infrared camera were used to heat the samples. After heating, up to 30 images were sequentially acquired at 70 - 150 msec intervals. Limits of detectability based on depth and diameter of the flat-bottom holes were defined for each composite material. Ultrasonic and radiographic images of the samples were obtained and compared with the thermographic images. This study was done under a non-reimbursable Space Act Agreement between NASA-Lewis Research Center and Bales Scientific, Inc. to allow several heating configurations to be evaluated in a cost-effective and timely fashion. The authors wish to thank Ron Cairo of Pratt & Whitney for delamination sensitivity analysis.				
14. SUBJECT TERMS Nondestructive evaluation; Thermography; Composites			15. NUMBER OF PAGES 26	
			16. PRICE CODE A03	
17. SECURITY CLASSIFICATION OF REPORT Unclassified	18. SECURITY CLASSIFICATION OF THIS PAGE Unclassified	19. SECURITY CLASSIFICATION OF ABSTRACT Unclassified	20. LIMITATION OF ABSTRACT	